Simulations of surfactant-laden drops rising in a density-stratified medium

David W. Martin* and François Blanchette
Applied Mathematics, University of California at Merced, 5200 N. Lake Road, Merced, California 95343, USA
(Received 21 April 2016; published 27 February 2017)

We present simulations of the effects of insoluble surfactant on drops rising in unstratified media and density-stratified media. We consider an oil drop rising in water, and we track surfactant concentration on the drop surface. We first consider a drop coated with insoluble surfactant rising through an unstratified ambient. The drop speed is computed for various Marangoni numbers, and inertial and surface diffusion effects are also examined. In the second setup, we compare clean and contaminated drops rising through a linear density-stratified fluid. The entrained buoyancy is computed for various density gradients, and the effects of inertia and Marangoni number are characterized. We find that the entrained fluid slows the drop in a manner comparable to a vertical shift in the ambient density gradient.

DOI: 10.1103/PhysRevFluids.2.023602

I. INTRODUCTION

In the 2010 Deepwater Horizon oil spill, millions of gallons of crude oil leaked from the ocean floor and rose toward the surface. As the oil rose, it encountered a stratified water column, which rendered accurate predictions of its location difficult. Moreover, in an effort to break down the oil, dispersants, including surfactants, were sprayed on the affected areas. A reliable description of the location of oil drops rising in the ocean thus requires the incorporation of both surfactant effects and density changes in the ocean. We present here a numerical study of both effects.

In the past century, a considerable number of studies have focused on the motion of drops, bubbles, and solid spheres in stratified and uniform ambients. Solid objects are usually assumed to be heavier than the surrounding liquid and so to settle under the influence of gravity, while bubbles are rising, propelled by buoyancy. Drops may be rising or settling depending on their density. However, the two cases are symmetric, and observations of rising drops apply in a symmetric fashion to settling drops. In this work, we consider drops that are lighter than the surrounding fluid, and thus we focus on rising drops.

In the inertia-free case, the speed of buoyancy-driven solid spheres [1] and drops and bubbles [2,3] has been calculated exactly. An approximate solution for flow past a solid sphere for low Reynolds number was obtained [4] using a singular perturbation analysis. A similar analysis was done for falling drops [5], including shape deformations due to inertia. The high Reynolds number case has been investigated experimentally [6] and analytically [7] assuming an irrotational velocity field.

Frumkin and Levich [8] (see also Refs. [9,10]) provided the theoretical framework for understanding surfactant effects on drop speed. Surfactants are surface-active agents that preferentially reside at fluid-fluid interfaces and affect the local surface tension. When a surfactant-laden drop rises in a uniform ambient, the surfactant is advected toward the rear of the drop, where it accumulates. As a consequence, surface tension decreases from the top to the bottom of the drop. The resulting tangential (Marangoni) stresses oppose the motion of the drop, thus decreasing its speed. Frumkin and Levich's work was subsequently confirmed by experimentalists, who observed velocity retardation for contaminated drops and bubbles [11–13]. In particular, Horton *et al.* [13] observed streak lines in rising drops using tracers and found that the flow detached from the drop surface toward the bottom, indicating stagnation there. Once a drop becomes sufficiently contaminated, the entire

*dmartin5@ucmerced.edu

surface becomes stagnant, and the drop behaves like a solid particle. In this regime, called uniform retardation, the speed of the moving drop will remain constant if the contamination is further increased.

More detailed experimental studies have since examined the steady-state speed of moving drops against the degree of surfactant contamination [14], drop shape [15], and desorption rate [16]. Numerous studies have calculated the steady-state velocity of a buoyancy-driven drop or bubble in the presence of surfactants, focusing on two main regimes. In the first regime, surface convection is much faster than sorption and bulk diffusion, so that the surfactant may be treated as insoluble. If, in addition, surface diffusion is negligible, there exists a region on the trailing end of the drop, called a stagnant cap, over which the surface is rendered immobile [17–19]. For the case of Stokes flow, an exact, closed form solution has been obtained for the linear [20] and nonlinear [21] surfactant relation.

In the second regime, sorption and bulk diffusion occur over the same time scale as convection. Several authors [22–24] have accounted for sorption from the bulk using boundary layer analysis valid for low bulk diffusion. Holbrook and Levan published a two-part study of the steady-state velocity of a buoyancy-driven drop in a surfactant bath, treating the stagnant cap limit and the limit of uniform retardation asymptotically [25] and treating the intermediate regime numerically [26]. This was generalized to the full Frumkin surfactant relation in Ref. [27], and Ref. [28] studied the effects of the bulk Péclet number on surfactant distribution for a variety of bulk concentrations. More recent studies have examined the effects of a finite Reynolds number with [29–31] and without [32,33] deformation and described the wake that forms behind the drop.

Nearly all studies of surfactant effects on moving drops and bubbles have focused on steady-state motion in a uniform ambient, although a few [34,35] have examined transient motion in a uniform ambient. Studies of settling in a stratified ambient have generally involved either surfactant-free drops and bubbles or solid, spherical balls. Extensive work [36–41] has been done studying the passage of drops and solid spheres through a layer between two immiscible fluids. In 1999 the first study [42] of drops passing through a density-stratified fluid observed increased drag due to fluid entrainment. In sufficiently sharp stratifications, falling balls were observed to reverse direction, temporarily levitating before passing into the lower layer [43]. In the Stokes limit, the velocity of a drop passing through a sharp stratification has been described theoretically [44,45]. For weakly stratified media, such as are found in nature, entrainment effects on the drag have been carefully quantified for solid spheres [46] and drops [47]. In this setup, drop deformation, oscillation, and the flow field have also been examined [47]. The transient motion of solid spheres settling in a linearly stratified fluid has also been studied [48]. Another substantial body of research concerns the plumes generated by bodies passing through a stratification (see, for example, Refs. [49–51]). Research has also been done concerning the oscillations of neutrally buoyant bodies [52,53]. Other recent studies [54,55] have examined porous bodies settling in stratified fluid, due to their value in modeling marine snow. One recent study [56] accounted for Marangoni effects due to compositional differences between two layers of miscible fluid. However, to the best of our knowledge, no studies have examined surfactant effects on drops rising in stratified media.

Here we present a numerical study of surfactant effects on rising drops as applicable to oil drops in the ocean. We consider both a uniform and a density-stratified ambient, and we seek to understand the combined effect of the surfactant and stratification on the drop velocity. Like the authors of Ref. [47], we quantify entrainment effects, but we combine them with surfactant effects and analyze these effects in terms of added buoyancy, rather than added drag. We examine a regime in which inertia is non-negligible, but where the drop remains approximately spherical, and we consider the insoluble regime. We would prefer to keep diffusion effects as small as possible. However, due to limitations of our numerical method, the effects of surface diffusion are non-negligible and are therefore quantified. In Sec. II we present the setup of our simulations and the equations governing the system. We discuss our numerical method and its validation in Secs. III and IV, respectively. Then we present our results for two setups: a surfactant-laden drop rising in a uniform ambient (Sec. V) and a surfactant-laden drop rising in a linear density-stratified fluid (Sec. VI).

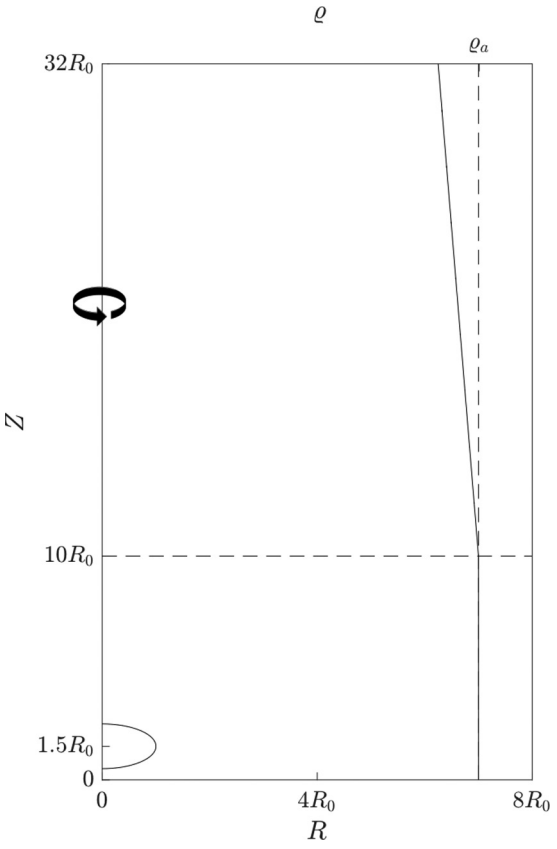

FIG. 1. The axisymmetric computational domain, scaled according to the drop radius, R_0. The drop is shown near the axis, and the ambient density, ϱ, is plotted to the right. The density-stratified fluid begins at $Z = 10R_0$.

II. SETUP AND GOVERNING EQUATIONS

We consider an axially symmetric system where a surfactant-laden drop is rising under the influence of buoyancy in a cylindrical container. We apply a no-slip boundary condition on the top, bottom, and side walls, but we keep the walls sufficiently far away as to not influence the dynamics of the rising drop. The computational domain, shown in Fig. 1, begins at the axis, and extends 8 drop radii in the radial direction and 32 drop radii in the vertical direction. Initially, the drop center is located 1.5 drop radii above the bottom wall. The drop is allowed to rise to terminal velocity before entering the layer of density-stratified fluid, which begins at 10 drop radii from the bottom of the container. The surface of the drop, $\mathbf{x}_s$, moves with the local fluid velocity $\mathbf{u}$:

$$\frac{d\mathbf{x}_s}{dt} = \mathbf{u}\Big|_{\mathbf{x}_s}. \tag{1}$$

The fluid is assumed Newtonian and incompressible, and so it is described by the incompressible Navier-Stokes equations. We nondimensionalize the equations using the drop radius, R_0, as a length scale and the drop density, ϱ_d, as a density scale. For a velocity scale, we use the Hadamard-Rybczynski speed [2,3] of a clean drop rising in creeping flow, assuming for simplicity that the drop and the ambient have the same viscosity, μ:

$$U_{\mathrm{HR}} = \frac{4g(\varrho_a - \varrho_d)R_0^2}{15\mu}. \tag{2}$$

Here g is the gravitational acceleration and ϱ_a the density of the ambient fluid at the bottom of the container (absent any stratifying agent). With this choice of scales, the Navier-Stokes equations can be written in dimensionless form as

$$\nabla \cdot \mathbf{u} = 0, \tag{3}$$

$$\rho \frac{\partial \mathbf{u}}{\partial t} + \rho \mathbf{u} \cdot \nabla \mathbf{u} = -\nabla p + \frac{1}{\mathrm{Re}} \nabla^2 \mathbf{u} + \frac{15}{4\mathrm{Re}} \Delta\rho \mathbf{k}, \tag{4}$$

where p is the dimensionless fluid pressure, ρ is the dimensionless fluid density, $\mathbf{k}$ is a vertical unit vector, and

$$\mathrm{Re} = \frac{\varrho_d R_0 U_{\mathrm{HR}}}{\mu} \tag{5}$$

is the Reynolds number, measuring inertial against viscous forces. In the momentum equation (4), the left-hand side contains the convective and advective derivatives of the momentum, and the right-hand side contains forcing terms—specifically the pressure gradient, viscous force, and buoyancy force. The buoyancy term depends on a normalized density difference between the drop and the ambient:

$$\Delta\rho = \frac{\varrho_a - \varrho_d \rho}{\varrho_a - \varrho_d} = \frac{\mathcal{D} - \rho}{\mathcal{D} - 1} \quad \text{where} \quad \mathcal{D} = \frac{\varrho_a}{\varrho_d}. \tag{6}$$

We track the surfactant concentration on the drop surface, γ, using an advection-diffusion equation restricted to the interface [57]. This can be expressed in dimensionless form using a Péclet number:

$$\frac{\partial \gamma}{\partial t} + \nabla_s \cdot (\gamma \mathbf{u}) = \nabla_s \cdot \left(\frac{1}{\mathrm{Pe}_\Gamma} \nabla_s \gamma \right) \quad \text{where} \quad \mathrm{Pe}_\Gamma = \frac{U_{\mathrm{HR}} R_0}{k_\gamma}. \tag{7}$$

The constant k_γ is is a diffusion coefficient on the drop surface. We denote a gradient tangential to the surface at $\mathbf{x}_s$ using ∇_s. The surfactant concentration is scaled by its initial uniform value, Γ_0.

For simplicity, we use a linear elasticity relation between surface tension, σ, and surfactant concentration on the surface [57,58], given in dimensionless form as

$$\sigma = 1 + \beta(1 - \gamma). \tag{8}$$

Here both surface tension and surfactant concentration are normalized by their equilibrium values, Σ_0, Γ_0. The elasticity coefficient, $\beta = -\partial\sigma/\partial\gamma$, written here in terms of the dimensionless surface tension and surface surfactant concentration, measures the rate of change of surface tension with changes in surfactant concentration. Writing β in terms of the dimensional surface tension Σ and surfactant concentration Γ, as $\beta = -(\Gamma_0/\Sigma_0)\partial\Sigma/\partial\Gamma$ reveals that β also depends on the equilibrium surfactant concentration and the surface tension scale.

The effects of surface tension on the dynamics of the system can be described as boundary conditions on the stress:

$$\mathbf{n} \cdot [\nabla \mathbf{u} + \nabla \mathbf{u}^T] \cdot \mathbf{n} = \frac{\mathrm{Re}}{\mathrm{We}} \sigma \kappa \mathbf{n}, \tag{9}$$

$$\mathbf{n} \cdot [\nabla \mathbf{u} + \nabla \mathbf{u}^T] \cdot \mathbf{t} = \frac{\mathrm{Re}}{\mathrm{We}} \nabla_s \sigma = -\mathrm{Mg} \frac{\partial \gamma}{\partial s}. \tag{10}$$

Here κ is the total (twice the mean) curvature, $\mathbf{n}$ is the unit normal to the surface, and $\mathbf{t}$ is the unit tangent in the direction of increasing s. The new dimensionless number appearing in both of Eqs. (9) and (10) is the Weber number, which measures inertia against surface tension and is given by

$$\mathrm{We} = \frac{\varrho_d R_0 U_{\mathrm{HR}}^2}{\Sigma_0}. \tag{11}$$

TABLE I. Definition and range of parameters in our simulations.

Parameter	Definition	Range	
		Sec. V	Sec. VI
Re	$U_{\mathrm{HR}} R_0 \varrho_d / \mu$	1,10	1,20
We	$U_{\mathrm{HR}}^2 R_0 \varrho_d / \Sigma_0$	0.05–0.2	0.05–0.2
β	$-\partial\sigma/\partial\gamma$	0–0.2	0–0.2
Mg	$\Sigma_0 \beta / \mu U_{\mathrm{HR}}$	0–2	0,2
$\mathcal{D}$	ϱ_a / ϱ_d	1.1	1.1
Pe	$U_{\mathrm{HR}} R_0 / k_\rho$	NA	10^4
Pe_Γ	$U_{\mathrm{HR}} R_0 / k_\gamma$	10,100	100
S	$-(R_0/\varrho_d)\partial\varrho/\partial Z$	0	5×10^{-4} to 5×10^{-3}

In this context, the Weber number quantifies shape deformation of the drop and is kept small (see Table I) so that the drop remains approximately spherical. In particular, in all our simulations the drop's aspect ratio varied by less than 2%. The expression on the far right of Eq. (10) is obtained by differentiating Eq. (8). The dimensionless number appearing there is the Marangoni number, defined by

$$\mathrm{Mg} = \frac{\beta \mathrm{Re}}{\mathrm{We}} = \frac{\Sigma_0 \beta}{\mu U_{\mathrm{HR}}} \sim \frac{\text{tangential stress}}{\text{viscous stress}}. \tag{12}$$

We do not enforce the boundary conditions (9) and (10) directly but instead supplement the right-hand side of the momentum equation (4) with a surface force, multiplied by a delta function. In particular, we use

$$\rho \frac{\partial \mathbf{u}}{\partial t} + \rho \mathbf{u} \cdot \nabla \mathbf{u} = -\nabla p + \frac{1}{\mathrm{Re}} \nabla^2 \mathbf{u} + \frac{15}{4\mathrm{Re}} \Delta\rho \mathbf{k} + \delta_s \mathbf{F}_s, \tag{13}$$

where δ_s is a delta function that is nonzero only on the surface, and

$$\mathbf{F}_s = \frac{1}{\mathrm{We}} (\sigma \kappa \mathbf{n} + \nabla_s \sigma). \tag{14}$$

In the presence of a stratifying agent, the density obeys an advection-diffusion equation, given, in dimensionless form, by

$$\frac{\partial \rho}{\partial t} + \mathbf{u} \cdot \nabla \rho = \frac{1}{\mathrm{Pe}} \nabla^2 \rho \quad \text{where} \quad \mathrm{Pe} = \frac{U_{\mathrm{HR}} R_0}{k_\rho}. \tag{15}$$

In the above Péclet number, k_ρ is the diffusion coefficient of density. We note that Eq. (15) applies only outside the drop; the fluid density is held constant inside the drop. We neglect diffusion inside the drop because we have in mind salt diffusion, which is negligible in oil over the time scale we consider. A Péclet number of $\mathrm{Pe} = 10^4$ is used. Péclet numbers associated to salt diffusivity in the ocean are typically much larger, but Péclet numbers greater than 10^4 are difficult to resolve numerically.

We consider two setups. Both setups involve a drop rising to terminal velocity in a uniform ambient with dimensionless density $\rho = \mathcal{D}$. In the first setup the drop maintains its terminal velocity in a uniform ambient, while in the second setup the drop enters a linear density-stratified fluid, beginning at $z = z_0$. The initial density of the ambient fluid is thus

$$\rho(z) = \begin{cases} \mathcal{D} & \text{if } z < z_0 \\ \mathcal{D} - S(z - z_0) & \text{if } z \geqslant z_0 \end{cases}, \tag{16}$$

where

$$S = -\frac{\partial \rho}{\partial z} = -\frac{R_0}{\varrho_d}\frac{\partial \varrho}{\partial Z}$$

is the gradient of the density, given in dimensionless form. Here ϱ and Z are the dimensional density and vertical position coordinate, respectively. The case of a uniform ambient is recovered by setting $S = 0$.

To facilitate keeping track of all the dimensionless numbers involved, we have summarized them all in Table I, along with their definitions and the range used for each setup considered.

III. NUMERICAL METHOD

We use a finite difference volume of fluid (VOF) method [59], in which the Navier-Stokes equations are solved on a staggered marker and cell (MAC) grid. The viscous and advection terms in the Navier-Stokes equations are computed using centered finite differences, and the system is advanced in time using an Euler time step. We use a projection method [60] to compute a pressure that automatically enforces continuity. This results in a Poisson equation for the pressure, which is solved using iterative methods.

We track the interface using markers that are advected with the fluid in a Lagrangian manner, via Eq. (1). Cubic splines are employed for interpolating between the markers and for computing a smooth curvature on the interface. The moving front is related to the fixed grid using linear interpolation. The markers are redistributed at every time step, to maintain a distance between markers of roughly one grid square. We eliminate parasitic currents by making corrections to account for the discontinuous pressure jump at the interface [61].

We track the surfactant using a Lagrangian approach that automatically conserves mass [62,63]. We begin by computing the mass m_k^{t-1} of surfactant near the kth marker at time $t-1$:

$$m_k^{t-1} = \gamma_k^{t-1}\Delta A(s^{t-1}), \tag{17}$$

where γ_k^{t-1} is the surfactant concentration at the kth marker, and ΔA_k^t represents the area of the interface associated to the k^{th} marker as a function of the arc length s^{t-1} at time $t-1$. On the axis, this is $\Delta A_k^t = \pi(\Delta s_k^t)^2$, and away from the axis, it is $\Delta A_k^t = 2\pi r_k^t \Delta s_k^t$, where r_k^t is the distance to the axis. After the markers are advanced, and a new arc length s^t is computed, but before the markers are redistributed, we update surfactant concentration to a temporary value γ_k^*, by inverting Eq. (17):

$$\gamma_k^* = m_k^{t-1}/\Delta A(s^t). \tag{18}$$

We then redistribute the markers so as to ensure that they remain equally spaced. We begin simultaneously at the top and bottom of the drop and leave the surfactant concentration at the first marker unchanged. We then move toward the center from one marker to the next, choosing the surfactant concentration of the redistributed kth marker so as to conserve the total surfactant mass up to that point. In particular, we choose a point $s_{k+1/2}$ midway between the kth marker and the $(k+1)$-st marker and compute the total mass $M_{k+1/2}^{\text{old}}$ from the poles of the drop to that point for the unredistributed markers. Then we choose a point $s_{k-1/2}$ midway between the $(k-1)$-st marker and the kth marker and compute the surfactant mass, $M_{k-1/2}^{\text{new}}$, up to that point. Last, we choose the redistributed concentration, γ_k, to enforce the condition

$$M_{k-1}^{\text{new}} + 2\pi r_k(s_{k+1/2} - s_{k-1/2})\gamma_k = M_k^{\text{old}}.$$

The second term on the left-hand side is the surfactant mass in an axially symmetric strip centered at the kth marker. For convenience, we choose the number of markers to be odd and choose the surfactant concentration at the middle marker (near the "equator") to conserve exactly the total surfactant mass on the drop. After redistributing, the new concentration is computed by adding a diffusive term, which is a finite difference discretization of the surface Laplacian ∇_s^2.

TABLE II. Variations in drop mass, ΔM_d, total energy, ΔE, and surfactant mass, ΔM_γ, against mesh size h. The number of time steps for which the simulation was run is also shown.

h	Time steps	ΔM_d	ΔE	ΔM_γ
1/4	689	0.0126	0.1077	0
1/8	2858	0.0061	0.0753	0
1/16	11 656	0.0020	0.0362	0
1/32	38 000	0.0010	0.0161	8.75×10^{-7}

Equation (15) is solved similarly to the Navier-Stokes, using centered differences and an Euler time step. To keep surfactant from diffusing across the fluid interface, we impose symmetric boundary conditions at the interface. We implement these conditions using a discrete approximation, $\Phi_{i,j}$ to the indicator function ϕ, which is unity in the drop and zero outside. The value of grid function $\Phi_{i,j}$ equals the percentage of the cell that is inside the drop. Whenever $\Phi_{i,j} \leqslant 0.5$, but adjacent cells have $\Phi_{i\pm1,j\pm1} > 0.5$, the values of the stratification agent in the adjacent cells are set equal to the value in cell i, j, which prevents the stratification outside the drop from diffusing into the drop. The resulting spurious stratification agent inside the drop is neglected in computing the fluid density, which is set to unity inside the drop.

IV. VALIDATION

A. Conservation properties

We begin by demonstrating that our method conserves drop mass M_d, surfactant mass, M_γ, and the total energy, E, of the system. Energy can be tracked using an energy budget [64] for a multiphase flow system involving two immiscible fluids. Conservation is demonstrated by convergence of the quantity

$$\Delta X = \frac{\max_t[X(t)] - \min_t[X(t)]}{X(0)}, \tag{19}$$

where $X(t)$ is $M_d(t)$, $M_\gamma(t)$, or $E(t)$. We tested the code by simulating a drop rising through a sharp density transition. For validation purposes, we used a cylindrical domain with a nondimensional radius of four, a height of eight, and a sharp density transition in the middle of the domain. In particular, $\rho(t = 0)$ transitions from 1.1 to 1.05 as z increases from 3.95 to 4.05.

The results, shown in Table II, show first order convergence for drop mass and energy conservation, as the mesh size is decreased from $h = 1/8$ to $h = 1/32$, where h is the width of one square cell in the MAC grid. Surfactant mass is conserved exactly, except when $h = 1/32$, where the failure of exact conservation can be explained by round-off error. All simulations performed in Secs. V and VI use $h = 1/32$.

B. Oscillations of an irrotational drop

The oscillations of a perturbed spherical drop have been calculated for the case in which the perturbation is small relative to the drop radius. For a liquid drop immersed in a gas of negligible density and viscosity, the second mode of frequency is given by [65]

$$\omega_2^2 = \frac{8\sigma}{\rho R_0^3}. \tag{20}$$

We ran simulations of a perturbed drop, measuring the primary mode of oscillation with an initial aspect ratio of 1.05, surrounded by a gas, whose density and viscosity are 10% of those of the drop. On a cylindrical domain of radius $2.5R_0$ and height $5R_0$, with $h = 5/512$, the computed oscillation frequency differed from the theoretical frequency by no more than 0.33%.

TABLE III. Error in scalar field mass conservation, defined in Eq. (19) (second column) against mesh width h (first column). The third column shows the duration of the simulation in dimensionless time, and the last column shows the order of convergence, defined as α, such that $\Delta M_f = O(h^\alpha)$.

h	ΔM_f	t	Order
1/4	3.73×10^{-4}	25.16	NA
1/8	3.68×10^{-5}	22.12	3.34
1/16	2.26×10^{-6}	20.70	4.02
1/32	1.93×10^{-7}	20.04	3.54

C. Conservation of the stratifying agent

We validate our method for tracking scalar fields by modeling a drop rising through a sharp density stratification and measuring how well the mass of the stratifying agent is conserved over time for different resolutions. For validation purposes, we use a small cylindrical domain with a radius of 4 drop radii and a height of 8 drop radii. After beginning our simulation with the drop a distance of 1.5 drop radii above the bottom of the container, we allow the drop to rise through a sharp density stratification at $z = 4$, and we stop the simulation when the drop is 1.5 radii away from the top of the container. In this validation, we allow the stratifying agent to diffuse in both the drop and the ambient, with a Péclet number of $\mathrm{Pe} = 4000$. The error in mass conservation is the percentage variation in the mass M_f of the scalar field, defined as a volume integral of the concentration function over the cylindrical domain. The results, shown in Table III show an objectively small error and better than second order convergence. The dimensionless time, t, of the simulation is also given.

V. A DROP RISING IN A UNIFORM AMBIENT

We begin by studying a drop covered with an insoluble surfactant moving a uniform medium. We have conducted simulations for Reynolds numbers of $\mathrm{Re} = 1, 10$ and surface Péclet numbers of $\mathrm{Pe}_\Gamma = 10, 100$. We compare our results to theoretical solutions in the limit case of zero Reynolds number and infinite Péclet number to highlight the effects of inertia and surface diffusion.

In the absence of sorption, and when $\mathrm{Pe}_\Gamma \gg 1$, Eq. (7) implies $\gamma \mathbf{u}_s = \mathbf{0}$ for a steadily rising drop [17]. There are thus only two possibilities along the drop surface: either the surface is locally clean ($\gamma = 0$), with a free-slip condition, or the surface is locally covered with surfactants and stagnant ($\mathbf{u}_s = \mathbf{0}$). In practice, surfactant is convected to the bottom of the drop where it forms a stagnant cap. The transition from a clean drop to the spherical cap takes place at some fixed angle, θ_c, traditionally measured from the bottom axis (see Fig. 2).

On the surface of the drop, viscous stresses drive the surfactant toward the base of the drop and are opposed by tangential stresses which seek to bring the surfactant into equilibrium. Balancing the two, one obtains the Marangoni number, Mg. When $\mathrm{Mg} \ll 1$, we expect Marangoni effects to be negligible, so that the drop behaves like a clean drop. On the other hand, when $\mathrm{Mg} \gg 1$, Marangoni effects will dominate viscous effects, forcing the surface velocity of the fluid to zero, so that the drop behaves like a solid sphere. We therefore expect the system to transition from clean drop behavior to solid sphere behavior as the Marangoni number increases above one.

Sadhal and Johnson [20] obtained exact solutions for the flow field, the surfactant distribution, and the drag coefficient as functions of the cap angle for an inertia-free, diffusion-free rising drop. The velocity U_{SJ} that they found is given by [20]

$$U_{\mathrm{SJ}} = \frac{U_{\mathrm{HR}}}{C_D(\theta)}, \tag{21}$$

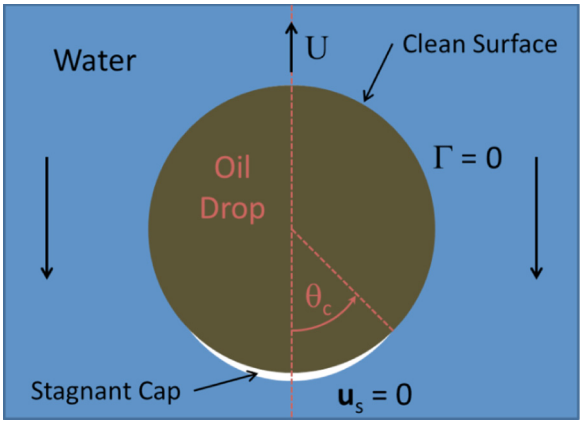

FIG. 2. A surfactant-laden drop rising in a uniform ambient, with negligible surface diffusion. The surfactant appears in white as a cap on the bottom of the drop, which transitions to a clean surface at a cap angle, θ_c.

where

$$C_D(\theta_c) = 1 + \frac{\mu_a}{2\pi(2\mu_a + 3\mu_d)}\left(2\theta_c + \sin\theta_c - \sin 2\theta_c - \frac{1}{3}\sin 3\theta_c\right) \tag{22}$$

is a drag coefficient that depends on the respective dynamic viscosities μ_a and μ_d of the ambient and drop, and U_{HR} is the familiar Hadamard-Rybczynski velocity of a rising drop in Stokes flow. They found that the surface tension as a function of angle is described by [20]

$$\frac{\partial \Sigma}{\partial \theta} = \mu_a U_{\mathrm{SJ}} h(\theta,\theta_c), \tag{23}$$

where

$$h(\theta,\theta_c) = \frac{2}{\pi}\tan\left(\frac{\theta}{2}\right)\left\{\frac{3}{2}(1+\cos\theta)\left[\arcsin\left(\frac{\cos\theta - \cos\theta_c}{1+\cos\theta}\right)^{1/2} + \frac{(\cos\theta - \cos\theta_c)^{1/2}(1+\cos\theta_c)^{1/2}}{1+\cos\theta}\right] + \frac{(1+\cos\theta_c)^{3/2}}{(\cos\theta - \cos\theta_c)^{1/2}}\right\}. \tag{24}$$

Equation (24) can be integrated analytically to get

$$H(\theta,\theta_c) = \int_{\theta_c}^{\theta} h(\psi,\theta_c)\,d\psi = -\frac{2}{\pi}\left[\left(\frac{3}{2}\eta - \eta_c\right)\arcsin\left(\frac{\eta-\eta_c}{\eta}\right)^{1/2} + \frac{3}{2}\sqrt{\eta_c(\eta-\eta_c)}\right], \tag{25}$$

where $\eta = 1 + \cos\theta$ and $\eta_c = 1 + \cos\theta_c$. This gives us an explicit formula for the surface tension on the stagnant cap:

$$\Sigma(\theta) = \Sigma_{\max} + \mu_a U_{\mathrm{SJ}}(\theta_c) H(\theta,\theta_c), \tag{26}$$

where $\Sigma_{\max}$ is the maximum surface tension, obtained on the clean part of the drop.

Putting Eq. (8) into Eq. (23) and integrating, we find the surfactant concentration

$$\frac{\Gamma(\theta)}{\Gamma_0} = -\frac{1}{\mathrm{Mg}}\frac{H(\theta,\theta_c)}{C_D(\theta_c)}. \tag{27}$$

The constant of integration was evaluated using the condition $\Gamma(\theta = \theta_c) = 0$, which is valid so long as the drop is not completely stagnant, i.e., $\theta_c < \pi$.

Figure 3 shows the computed and theoretical surfactant distributions of a steadily rising drop plotted against the angle measured from the bottom of the drop. As expected, surface diffusion

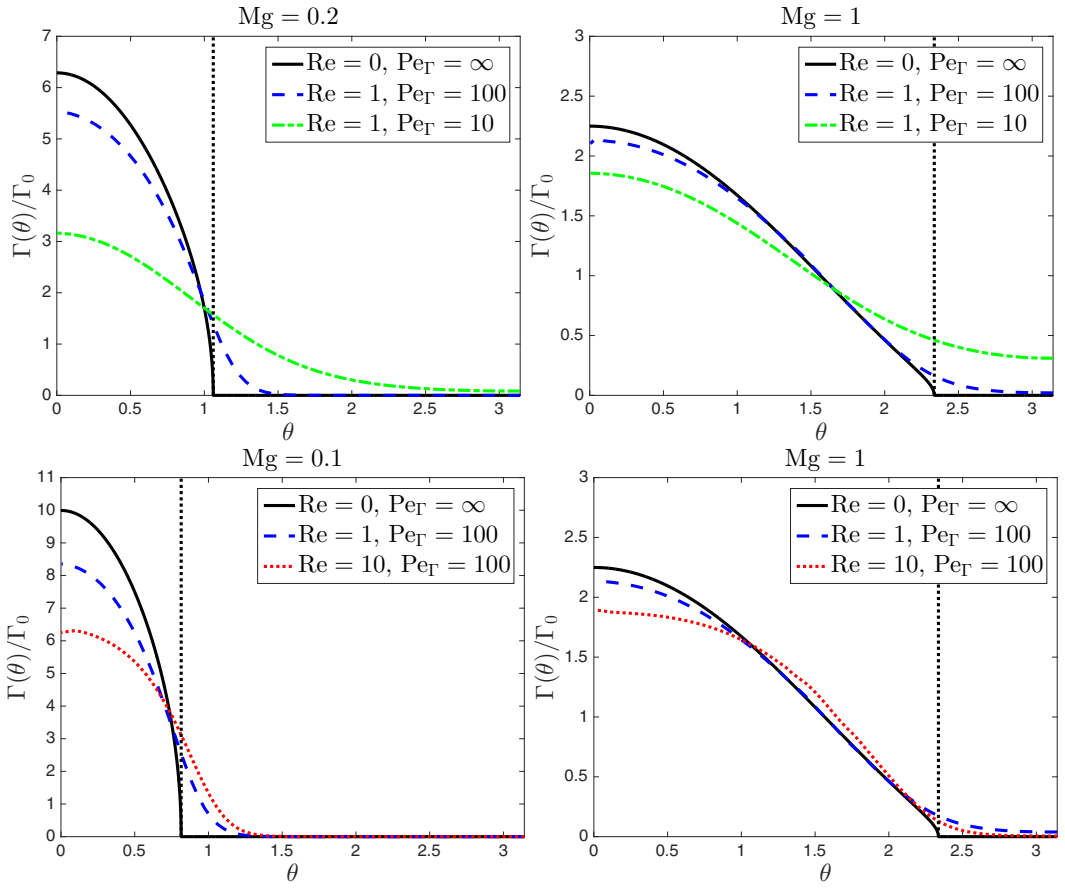

FIG. 3. Surfactant distribution against angle from the bottom of the drop, for different Reynolds numbers, Péclet numbers, and Marangoni numbers. The solid black line shows the theoretical distribution, while the dashed and dotted colored curves show computed distributions. The cap angle, θ_c, is shown as a vertical black dotted line.

(inverse Péclet number) smooths out the surfactant distribution. Otherwise, the agreement between the theoretical and computational surfactant profiles is excellent. Inertial effects tend to reduce the departure from a uniform surfactant distribution. For $\mathrm{Mg} = 1$, the effect is relatively weak: for $\mathrm{Re} = 10$, the concentration departed from the inertia-free case, shown by the solid black line in the figures, by no more than 20%, decreasing at the pole and increasing slightly at the equator. For $\mathrm{Mg} = 0.1$, the effect is larger, resulting in a significant redistribution of surfactant from the bottom of the drop toward its sides.

Integrating Eq. (27) over the surface of the drop, we obtain a formula for the total surfactant mass:

$$M_\gamma(\theta_c) = -\frac{2\pi R_0^2 \Gamma_0}{\mathrm{Mg} C_D(\theta_c)} \int_0^{\theta_c} H(\theta,\theta_c) \sin\theta \, d\theta = \frac{\Gamma_0 R_0^2 (2\theta_c - 4\theta_c \cos\theta_c - \sin 2\theta_c + 4\sin\theta_c)}{\mathrm{Mg} C_D(\theta_c)}. \quad (28)$$

Although Ref. [20] derived this formula, they did not present Eqs. (25)–(27) for the surfactant and surface tension distribution. An alternate expression for the total surfactant mass comes from considering the drop at rest (equilibrium). Then the surfactant is uniformly distributed and $M_\gamma(\theta_c) = 4\pi R_0^2 \Gamma_0$. Equating the two expressions for total surfactant mass, we obtain a formula for the

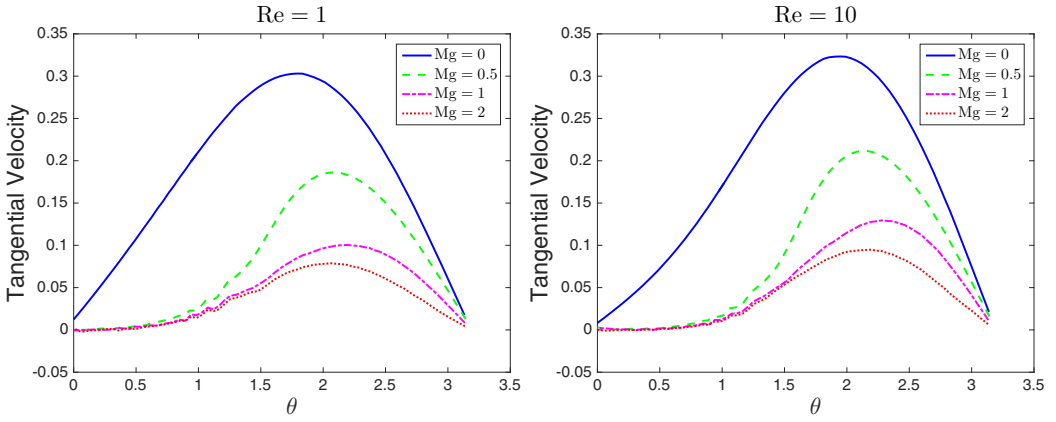

FIG. 4. Tangential velocity against angle from the bottom of the drop, for different Marangoni numbers and Reynolds numbers.

Marangoni number in terms of the cap angle:

$$\mathrm{Mg} = \frac{2\theta_c - 4\theta_c \cos\theta_c - \sin 2\theta_c + 4\sin\theta_c}{4\pi C_D(\theta_c)}. \tag{29}$$

Equation (29) can be inverted numerically to obtain the surfactant distribution and steady-state speed as functions of the Marangoni number.

Figure 4 shows the tangential velocity profiles of a drop rising in a uniform ambient for differing Reynolds and Marangoni numbers. The velocity profiles for $\mathrm{Re} = 1$ and $\mathrm{Re} = 10$ are similar, except that for the larger Reynolds number, the velocity peaks closer to the top of the drop, due to inertial effects. For Marangoni number $\mathrm{Mg} > 0$, we see the effect of the stagnant cap in suppressing the tangential velocity toward the bottom of the drop. As the Marangoni number increases, the tangential velocity on the entire drop decreases dramatically. For $\mathrm{Mg} = 2$, we expect the drop to be nearly stagnant. The flow that is present can be explained by diffusive effects ($\mathrm{Pe}_\Gamma = 100$), which smooth out the surfactant gradients that suppress flow on the surface. The noise that is visible on the velocity profile can be explained by small errors in computing the tangential velocity. This effect is due to the fact that the velocity decreases rapidly near the surface of the drop. Since we related the velocity field to the front using bilinear interpolation, this introduces a noticeable error.

Figure 5 shows theoretical and computational steady-state speeds of a drop rising in a uniform ambient, measured as departures from the surfactant free case ($\mathrm{Mg} = 0$). They are plotted against the Marangoni number, Mg, for varying Reynolds and Péclet numbers. We see that surfactant effects are inhibited at larger Reynolds numbers. This can be explained by considering the drag on the drop. Surfactant on the drop surface increases drag by partially immobilizing the surface, thus creating a no-slip boundary condition there for the ambient fluid. Increased viscosity favors increased drag by causing a larger volume of exterior fluid to be affected by the drop motion. If the Reynolds number were to become very large, a boundary layer of decreasing width would form around the region region of stagnation, the width of which would measure the amount of fluid being affected by the no-slip condition there. Thus, for smaller Reynolds numbers, such as we consider here, it is to be expected that the effect of the stagnant cap on the drop speed decreases with Reynolds number. McLaughlin [30] presents evidence that this trend reverses for larger Reynolds numbers ($\mathrm{Re} > 100$), due to the formation of large wakes. In our simulations, no wake was observed for $\mathrm{Re} \leqslant 10$ and $\mathrm{Mg} \leqslant 2$.

On the other hand, surface diffusion, measured by $1/\mathrm{Pe}_\Gamma$, counters the effect of the Marangoni number, so that the transition from a clean drop to a stagnant surface is much slower. This is to be expected, since surface diffusion smooths out the surfactant distribution, as seen in Fig. 3. For a

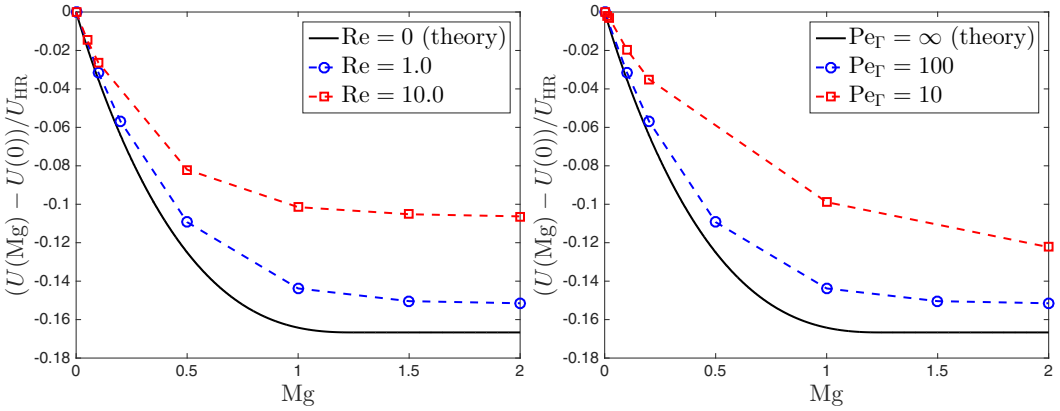

FIG. 5. Steady-state speed of surfactant-laden drops against Marangoni number, Mg, in a uniform ambient, for various Reynolds numbers (left) and surface Péclet numbers (right). For the computed results on the left, $\mathrm{Pe}_\Gamma = 100$; for the computed results on the right, $\mathrm{Re} = 1$. In the theoretical case (solid black) the Reynolds number is given by $\mathrm{Re} = 0$ and the Péclet number on the surface is given by $\mathrm{Pe}_\Gamma = \infty$.

smoother distribution, the surface tension gradient, $\partial\sigma/\partial\theta$, is decreased, resulting in an equivalent decrease in tangential stress. Since the tangential stress acts to reduce the rising speed, a lower Péclet number will result in an increased rising speed. In the absence of surface diffusion, the tangential stress increases with the Marangoni number, so that the effect of surface diffusion is to counteract the Marangoni effect.

For completeness, we also record the rising speed of clean drops for different Reynolds numbers (Table IV). We note that although the terminal speed of a clean drop varies significantly with the Reynolds number, the terminal speed of a contaminated drop ($\mathrm{Mg} = 2$) remains approximately 80% of the clean drop speed. In the theoretical case, this ratio is exactly $5/6 = 83.\overline{3}\%$. We expect that the difference between our computed results and the theory is due to wall effects and possibly surface diffusion.

VI. ENTRAINMENT EFFECTS IN A FLUID WITH LINEARLY STRATIFIED DENSITY

The terminal speed of a rising drop is proportional to the density difference between the drop and the ambient. The speed of a drop rising in a density-stratified fluid can therefore be expected to decrease with the density gradient, S. This effect is amplified by the process of entrainment, where a rising drop lifts heavier fluid into the lighter overlying ambient fluid, which further decreases the drop speed [44]. If the change in ambient density is sufficiently sharp, the direction of motion may even reverse [43].

We set $t = 0$ to correspond to when the center of the drop reaches the level $z = z_0$. The density gradient S is chosen so that the drop never reaches its neutral buoyancy level. We simulate various Reynolds numbers ($\mathrm{Re} = 1, 20$), Marangoni numbers ($\mathrm{Mg} = 0, 2$), and density gradients

TABLE IV. Speed relative to the Hadamard-Rybczynski speed for a clean drop (second column) and a contaminated drop (third column). The fourth column shows the ratio of a contaminated to clean drop speed.

Re	$U_{\mathrm{clean}}/U_{\mathrm{HR}}$	$U(\mathrm{Mg}=2)/U_{\mathrm{HR}}$	$U(\mathrm{Mg}=2)/U_{\mathrm{clean}}$
1	0.7486	0.6016	0.8036
10	0.5501	0.4438	0.8068
20	0.4723	0.3705	0.7845

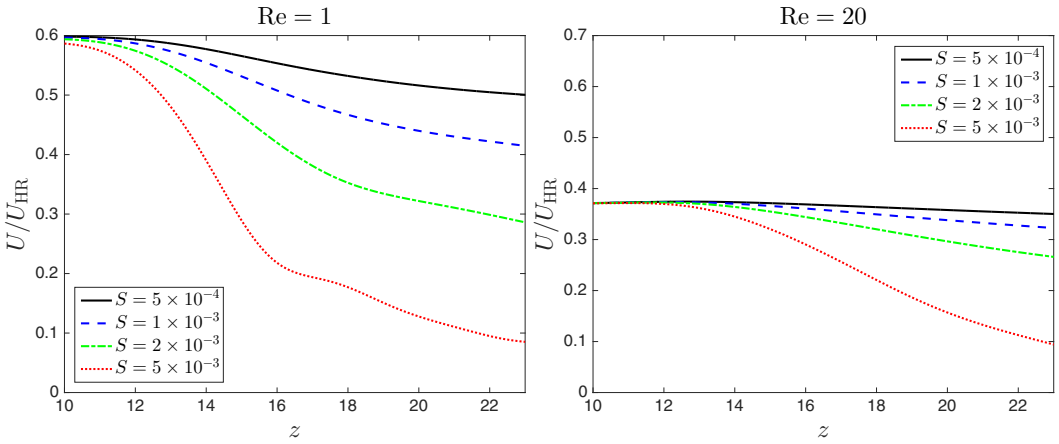

FIG. 6. The dimensionless speed, U/U_{HR}, of a drop rising in a linear density-stratified fluid, plotted against the vertical position coordinate, z, for different stratifications, and Reynolds numbers of $\mathrm{Re} = 1$ (left) and $\mathrm{Re} = 20$ (right). In all cases, $\mathrm{Mg} = 2$. The linearly stratified fluid begins at $z = 10$ and continues throughout.

($5\times10^{-4} \leqslant S \leqslant 5\times10^{-3}$). All Péclet numbers were kept as large as numerically feasible ($\mathrm{Pe}_\Gamma = 100$ and $\mathrm{Pe} = 10^4$).

Velocity profiles of the rising drops are shown in Fig. 6. The velocity profiles were smoothed using a Gaussian filter, to eliminate small-scale noise, which arises due to numerical imprecisions in computing the time derivative of the position of the drop's center of mass on a discrete grid and has a scale of roughly 5×10^{-4} when $h = 1/32$. Sharper stratifications favor decelerations of the rising drop. For a smaller Reynolds number, the drop undergoes a quicker and more dramatic shift in speed. In all cases, the drop transitions to a state of steady deceleration.

We show in Fig. 7 the derivative $du/dz = (R_0/U_{\mathrm{HR}})\,dU/dZ$ of the drop speed. In all cases, du/dz is near 0 when the drop enters the stratified fluid, and undergoes decaying oscillations after, relaxing toward a fixed negative value. The magnitude of these oscillations increases with S and decreases with the Reynolds number. To better quantify the transition to a steady deceleration, we examined the inflection points given by the first local minimum of du/dz after entering the

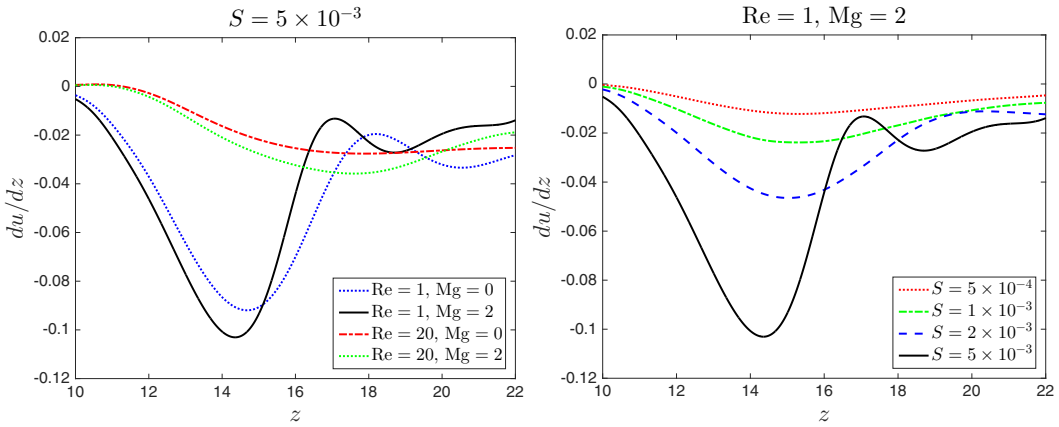

FIG. 7. The derivative, $du/dz = (R_0/U_{\mathrm{HR}})\,dU/dZ$, of the speed of a drop rising in a linear density-stratified fluid against position, for different Reynolds numbers and Marangoni numbers (left) and for different density stratifications (right). The stratified fluid begins at $z = 10$ and continues throughout.

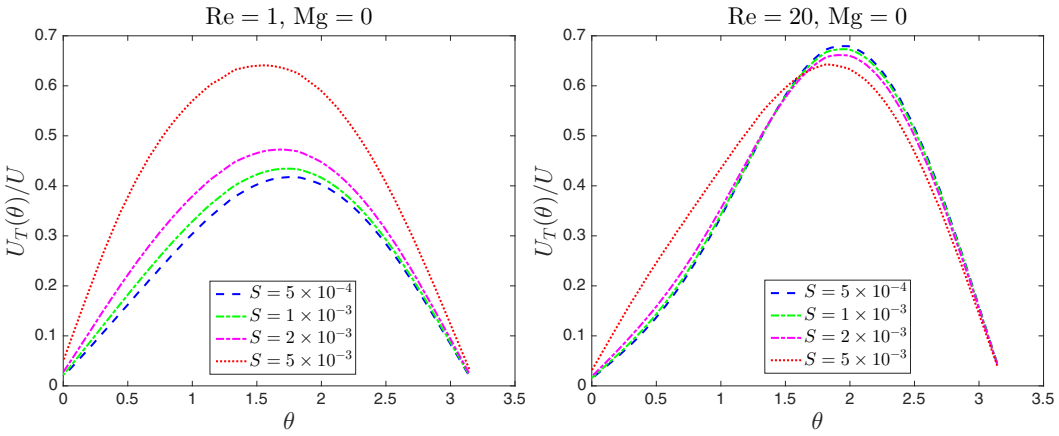

FIG. 8. Tangential velocity normalized by the speed of the drop against angle from the bottom of the drop, for different stratifications and Reynolds numbers. All profiles are taken at a height of $Z = 24$.

stratified fluid and measured the vertical distance above the beginning of the stratified fluid, z_t, where these inflection points occur. As can be seen in Fig. 7, z_t depends only weakly on the density gradient and Marangoni number. However, it depends strongly on the Reynolds number: for $\mathrm{Re} = 1$, $z_t \approx 4.8 \pm 0.6$, and for $\mathrm{Re} = 20$, $z_t \approx 8 \pm 0.5$. This can be understood by noting that the increased inertia associated to larger Re is expected to delay the transition as the drop maintains its original rising speed for longer.

Figure 8 shows tangential velocity profiles, $U_T(\theta)$, of drops rising through a linear density stratification normalized by the speed U of the rising drop. Because the drop speed is nonconstant in this case, we plotted all of the tangential velocity profiles at the same height, $Z = 24$, which in all cases occurs after the drop has entered a steady deceleration, but before wall effects are present. The normalized difference between the maximum tangential velocity and the drop speed, given by $1 - \max[U(\theta)]/U$, is due to fluid entrainment by the drop, and can be viewed as a crude measure of fluid entrainment. By this measure, we see that the amount of entrainment is greater for a smaller Reynolds number, Re, and that when $\mathrm{Re} = 1$, fluid entrainment decreases significantly for very large density gradients. When $\mathrm{Re} = 20$, there is no significant difference in entrainment associated to different density gradients, and instead, inertial effects appear dominant. In particular, in the presence of a steeper gradient, the tangential velocity distribution is more symmetric, presumably because the drop velocity is lower, resulting in weaker inertial effects.

Figure 9 shows surfactant profiles of drops rising through a linear density stratification, plotted when the drop center is at a height of $Z = 24$. The surfactant distribution from the stagnant cap theory for a uniform ambient in the limit of zero diffusion and Reynolds number is included for reference [20]. As in the case of the uniform ambient, the effect of the Reynolds number is to increase the surfactant mass at the equator of the drop and decrease it near the top and bottom. When the stratification is increased, the surfactant distribution becomes more uniform, which is presumably a consequence of the decreased drop velocity.

The effects of entrainment can be isolated by comparing full simulations to entrainment-free simulations. We obtained velocity profiles of rising drops in the absence of entrainment by running simulations where the ambient density varied with height but was kept constant in time (no advection). Figure 10 shows velocity profiles with and without entrainment. The rise of a drop with and without entrainment can also be compared directly by looking at the video provided as supplementary material for this paper [66]. In the latter case, the drop quickly assumes a steady deceleration after entering the stratified fluid. When entrainment is included, the drop first undergoes a transitional decrease in velocity before reaching nearly the same steady deceleration as in the entrainment-free

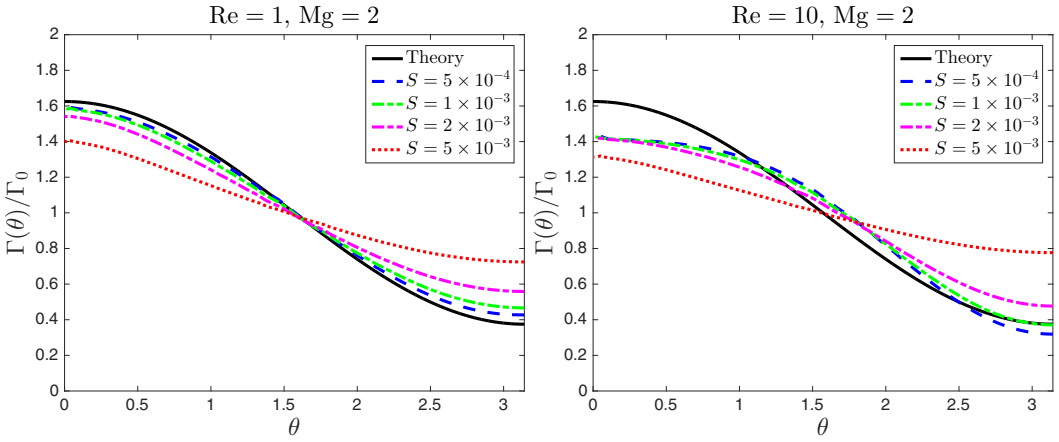

FIG. 9. Surfactant distribution against angle from the bottom of the drop, for different stratifications and Reynolds numbers. The theoretical case (solid black) refers to the stagnant cap theory for diffusion and Reynolds number equal to zero, in an unstratified ambient. All surfactant distributions were measured at a drop height of $Z = 24$.

case. This results in a net velocity lag

$$\Delta U = U_{\text{without entrainment}} - U_{\text{with entrainment}} = U_f - U$$

that is approximately constant once the transient phase is complete. We computed ΔU as the difference of the average velocity with and without entrainment, over an interval in the steady deceleration phase.

In Fig. 11 the relative velocity lag, $\Delta u = \Delta U / U_{\text{HR}}$, is plotted against the density gradient, S, for various Reynolds and Marangoni numbers. The relation is approximately linear. The slopes, b, of the lines $\Delta u = bS$ in Fig. 11 are presented in Table V. This linear relation fails for larger S, and the dependence of Δu on S becomes sublinear. As the drops rises, the drop and the fluid it entrains act together as a rising body with an intermediate average density. The difference between this mean density and the ambient density increases with stratification, and so it is expected that the velocity

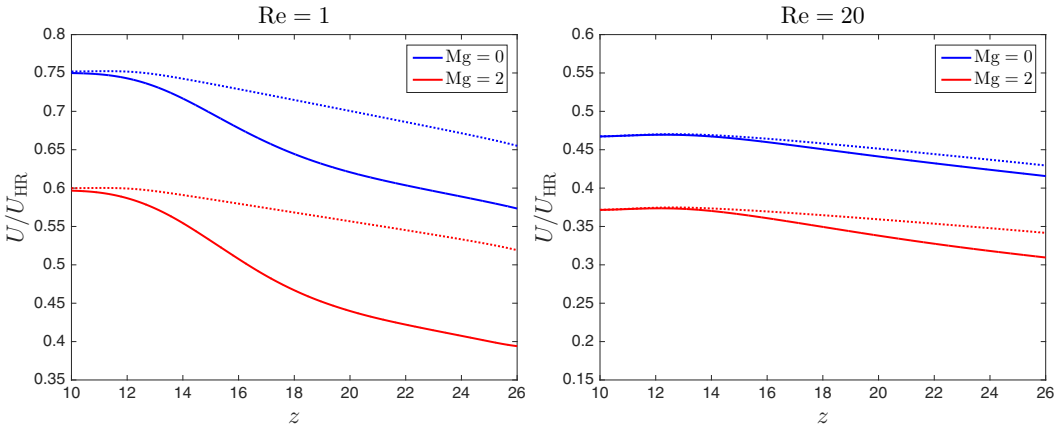

FIG. 10. The speed U/U_{HR} of a drop rising in a linear density-stratified fluid, plotted against the vertical position coordinate, z, with entrainment (solid line), and without entrainment (dashed line). Each figure shows two Marangoni numbers: Mg = 0,2. In both cases, $S = 10^{-3}$.

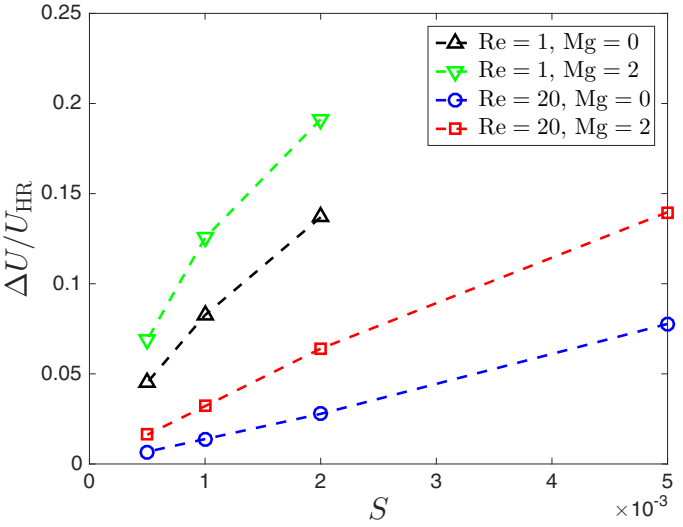

FIG. 11. The lag, $\Delta U/U_{\mathrm{HR}}$, in the speed of a drop rising in a stratified ambient due to entrainment effects, against the dimensionless density gradient of the fluid.

lag is proportional to the density gradient. When the stratification becomes sufficiently sharp, the drop begins to entrain a smaller volume of fluid, resulting in a sublinear relation between Δu and S. We also find that the velocity lag is greater for larger Marangoni number and smaller Reynolds number. In both cases, this is to be expected because the drop entrains more fluid.

The velocity lag, $\Delta U/U_{\mathrm{HR}}$, can be explained by a loss in buoyancy due to the entrainment of lighter fluid. In particular, we define the buoyancy lag due to entrainment as $F_e = F_d - F_{\mathrm{eff}}$, where F_d is the buoyancy of the drop and F_{eff} is the effective buoyancy of the system. The effective buoyancy balances the drag of the fluid so that the system achieves a quasi-steady state of slow deceleration. Altogether,

$$F_e = gV_d\varrho_d[\rho(z) - 1] - \mu R_0 U f(\mathrm{Re},\mathrm{Mg}), \tag{30}$$

where U is the (dimensional) drop speed, f is a dimensionless function of the Reynolds and Marangoni numbers, V_d is the volume of the drop, and $\rho(z) = \mathcal{D} - S(z - z_0)$ is the dimensionless ambient density [Eq. (16)]. The first term on the right-hand side of Eq. (30) is the drop buoyancy, F_d, while the second term is the drag on the drop.

In the absence of entrainment, $F_e = 0$, so that

$$0 = gV_d\varrho_d[\rho(z) - 1] - \mu R_0 U_f f(\mathrm{Re},\mathrm{Mg}), \tag{31}$$

TABLE V. The factor, $\zeta = b/a$, in the buoyancy lag, for the different Marangoni and Reynolds numbers studied. The slopes, b, of the lines in Fig. 11 are also given.

Re	Mg	b	$\zeta = b/a$
1	0	748	11.23 ± 0.07
1	2	1130	21.8 ± 1.9
20	0	140	3.55 ± 0.03
20	2	318	9.78 ± 0.25

where U_f is the velocity of a drop rising in an artificially fixed ambient. In that case, the drop velocity is given by the slopes, aS, of the dotted lines in Fig. 10. In particular, U_f satisfies $U_f(z)/U_{\rm HR} = U_0/U_{\rm HR} - aSz$, where the constant $a = gV_d\varrho_d/\mu R_0 f U_{\rm HR} = 5\pi\varrho_d/(\varrho_a - \varrho_d)f$ depends only on the Reynolds and Marangoni numbers, through the drag term, f. If we assume that the dependence of the drag on the Reynolds and Marangoni numbers takes the same form irrespective of entrainment, then f is the same with and without entrainment. Hence, we can subtract Eq. (31) from Eq. (30) to get

$$F_e = \mu R_0 \Delta U f(\mathrm{Re},\mathrm{Mg}) = \frac{gV_d\varrho_d\Delta U}{aU_{\rm HR}}. \tag{32}$$

The data in Fig. 11 suggest a linear relation between the velocity lag and the density gradient: $\Delta U/U_{\rm HR} = bS$ where b is a dimensionless constant. Altogether,

$$F_e = gV_d\varrho_d\frac{bS}{a}. \tag{33}$$

The ratio b/a that characterizes the buoyancy lag is identical to the horizontal separation ζ, between the solid and dotted curves in Fig. 10. Assuming both lines have the same slope, the quantity ζ is well defined and represents the additional distance the drop needs to rise before reaching the velocity it would have attained without entrainment. The fluid velocity, with and without entrainment, can be written as

$$U(z)/U_{\rm HR} = U_e/U_{\rm HR} - aSz \quad \text{and} \quad U_f(z)/U_{\rm HR} = U_0/U_{\rm HR} - aSz,$$

respectively, where U_e and U_0 are fixed velocities, satisfying $\Delta U = U_0 - U_e$. To compute the horizontal separation, ζ, we choose fixed vertical positions, z_e and z_f, such that $U(z_e) = U_f(z_f)$. Then

$$\zeta \equiv z_f - z_e = \frac{\Delta U}{aSU_{\rm HR}} = \frac{bS}{aS} = \frac{b}{a}.$$

The values of b computed from our simulations, as well as the length scale ζ are given in Table V. We see that entrainment is much more significant for low Reynolds numbers. In addition, entrainment is increased at larger Marangoni numbers, which is consistent with the observation that solid objects, with a no-slip condition similar to that of surfactant-covered drops, entrain more than liquid droplets [56].

VII. CONCLUSION

Using a VOF front-tracking method, we have studied numerically rising surfactant-laden drops, examining two cases likely to be relevant to oil drops in the ocean: a drop rising in a uniform ambient, and one entering a linear density-stratified fluid. In a uniform ambient, theoretical results are available for creeping flow, and we obtained good agreement with those results at low Reynolds number. We expanded existing work on surfactant-laden drops rising in a uniform ambient by accounting for surface diffusion and by examining Reynolds numbers in the range $1 \leqslant \mathrm{Re} \leqslant 20$. Our results thus complement existing results that focus either on relatively large Reynolds numbers ($\mathrm{Re} \geqslant 50$) [29–33] or very small Reynolds numbers ($\mathrm{Re} < 1$) [33]. We have also provided an explicit formula for the surfactant distribution on the surface of a drop in the Stokes limit of the stagnant cap regime. The effect of surfactants on the drop dynamics are largely the result of the formation of a stagnant cap on the lower portion of the rising drop. This cap generally increases the amount of fluid entrained by the drop. However, this additional resistance due to surfactants is weakened by fluid inertia, as entrainment decreases with increasing Reynolds number. Surface diffusion, characterized by a surface Péclet number, was also found to reduce the impact of surfactants, by spreading the surfactant over the interface, and allowing weak flow in the theoretically stagnant cap, resulting in weaker surface tension gradients.

No theoretical results are available for comparison when drops entered a density gradient, as can be found in the oceans. We observed in our simulations a transition from a steady velocity before entering the density gradient to a steady deceleration within it. This steady deceleration is due to the progressive reduction of the buoyancy difference between the drop and the ambient. However, the instantaneous speed of the drop lagged behind what one would expect from an unperturbed density profile, owing to the entrainment of heavy fluid by the drop. This velocity lag was observed to increase linearly with the density gradient, and was greatest for small Reynolds number and large Marangoni numbers. Moreover, the length of the transition region between the constant entry speed and the region of steady deceleration was found to increase with Reynolds number. The accurate description of the dynamics of a rising drop obtained here provides a valuable tool to predict the progression of surfactant-laden drops released in ambients with complicated density profiles. The concept of buoyancy lag, introduced here, similar to that of added mass, may also be used to describe settling of other particles in stratified ambients (e.g., nonspherical drops or solid particles, porous particles) to provide a simple measurement of the importance of entrainment. Previous authors [46] used the concept of added drag to explain the retardation of the motion of spherical particles in a linear stratification. Given that the steady deceleration of a drop or particle through a linear stratification is described by a balance of buoyancy and drag, the two concepts are related and may in practice be equivalent.

We have computed tangential velocity profiles for drops moving through uniform and density-stratified ambients. In the case of a uniform ambient, we quantified the role of surfactant in creating a stagnant cap on the surface of the drop, as well as the role of diffusion in offsetting that effect. Our findings are consistent with existing results for spherical bubbles [28,32–35] and for sorption-controlled surfactant-laden drops [27]. For a density-stratified ambient, we examined the tangential velocity profile relative to the drop speed and noted that the difference between the maximum tangential velocity and the drop velocity serves as an approximate measure of the amount of fluid entrained. It may be possible to construct a more accurate measure of entrainment using tangential velocities, in particular, by looking at an average of the vertical component of the tangential velocity. Given that the amount of fluid entrained is difficult to define, such a measure may actually provide a quantitative definition of entrainment in this case.

One important future extension of this work will be to connect our results for low Reynolds number with existing results [29–33] for intermediate Reynolds number. As inertial effects become important, the wake behind drops may become significantly more complex [29,30]. This in turns has consequences when considering suspensions where several drops interact. While it is a natural first step to consider a single drop, as we have done here, it is important to understand how rising drops will interact and the impact surfactants will have in such systems, as oil spills result in large numbers of drops rising together.

In natural systems, oil drops are eventually degraded by microorganisms. However, the flow around rising drops affects the ease with which microorganisms can reach the drop's surface. Quantifying the accessibility of drops may be done via direct simulations that include swimming organisms, or by more theoretical considerations, such as the rate of change of the stream function around the drop. To determine the best long-term approach to managing oil spills, it will also be important to investigate how surfactants affect the likelihood that oil drops will be degraded as they rise in the oceans.

Finally, while we have treated the limit case of insoluble surfactants, there is also an important regime in which the rate of sorption (adsorption and desorption) of surfactants needs to be considered. In typical applications, drops are generated by the break-up of large oil masses and thus start rising while virtually surfactant-free. As they encounter surfactants, their dynamics will change, but if the sorption takes place on the same time scale as the drop motion, opposing effects will compete. The characterization of the impact of sorption will be a significant step in providing a complete description of the rising of oil drops in a complex environment.

[1] G. G. Stokes, *Mathematical and Physical Papers* (Cambridge University Press, Cambridge, 1901), Vol. III.
[2] J. S. Hadamard, Mouvement permanent lent d'une sphère liquide et visqueuse dans un liquide visqueux, C. R. Acad. Sci. **152**, 1735 (1911).
[3] W. Rybczynski, Über die fortschreitende Bewegung einer flüssigen Kugel in einem zähen Medium, Bull. Acad. Sci. Cracovie A 40 (1911).
[4] I. Proudman and J. R. A. Pearson, Expansions at small Reynolds numbers for the flow past a sphere and a circular cylinder, J. Fluid Mech. **2**, 237 (1957).
[5] T. D. Taylor and A. Acrivos, On the deformation and drag of a falling viscous drop at low Reynolds number, J. Fluid Mech. **18**, 466 (1964).
[6] W. L. Haberman and R. K. Morton, An experimental investigation of the drag and shape of air bubbles rising in various liquids, Technical report, David Taylor Model Basin, Washington DC, 1953.
[7] D. W. Moore, The rise of a gas bubble in a viscous liquid, J. Fluid Mech. **6**, 113 (1959).
[8] A. Frumkin and V. Levich, On surfactants and interfacial motion, Zhur. Fiz. Khim. **21**, 1183, (1947).
[9] V. G. Levich, *Physicochemical Hydrodynamics* (Prentice Hall, New York, 1962).
[10] D. A. Edwards, H. Brenner, and D. T. Wasan, *Interfacial Transport Processes and Rheology* (Butterworth-Heinemann, Oxford, 1991).
[11] F. H. Garner and A. H. P. Skelland, Some factors affecting droplet behavior in liquid-liquid systems, Chem. Eng. Sci. **4**, 149 (1955).
[12] E. R. Elzinga and J. T. Banchero, Some observations on the mechanics of drops in liquid-liquid systems, Am. Inst. Chem. Eng. J. **7**, 394 (1961).
[13] T. J. Horton, T. R. Fritsch, and R. C. Kintner, Experimental determination of circulation velocities inside drops, Can. J. Chem. Eng. **43**, 143 (1965).
[14] R. M. Edge and C. D. Grant, The motion of drops in water contaminated with a surface-active agent, Chem. Eng. Sci. **27**, 1709 (1972).
[15] T. Yamamoto and T. Ishii, Effect of surface active materials on the drag coefficients and shapes of single large gas bubbles, Chem. Eng. Sci. **42**, 1297 (1987).
[16] K. J. Stebe, S.-Y. Lin, and C. Maldarelli, Remobilizing surfactant retarded fluid particle interfaces. I. Stress-free conditions at the interfaces of micellar solutions of surfactants with fast sorption kinetics, Phys. Fluids **3**, 3 (1991).
[17] P. Savic, *Circulation and distortion of liquid drops falling through a viscous medium*, National Research Council Canada, 1953.
[18] R. E. Davis and A. Acrivos, The influence of surfactants on the creeping motion of bubbles, Chem. Eng. Sci. **21**, 681 (1966).
[19] J. F. Harper, On bubbles with small immobile adsorbed films rising in liquids at low Reynolds numbers, J. Fluid Mech. **58**, 539 (1973).
[20] S. S. Sadhal and R. E. Johnson, Stokes flow past bubbles and drops partially coated with thin films. Part 1. Stagnant cap of surfactant film: Exact solution, J. Fluid Mech. **126**, 237 (1983).
[21] Z. He, C. Maldarelli, and Z. Dagan, The size of stagnant caps of bulk soluble surfactant on the interfaces of translating fluid droplets, J. Colloid Interface Sci. **146**, 442 (1991).
[22] B. V. Deryagin, S. S. Dukhin, and V. A. Lisichenko, The kinetics of the attachment of mineral particles to bubbles during flotation. I. The electric field of a moving bubble, Russ. J. Phys. Chem. **33**, 389 (1959).
[23] D. A. Saville, The effects of interfacial tension gradients on the motion of drops and bubbles, Chem. Eng. J. **5**, 251 (1973).
[24] J. F. Harper, On spherical bubbles rising steadily in dilute surfactant solutions, Q. J. Mech. Appl. Math. **27**, 87 (1974).
[25] J. A. Holbrook and M. D. Levan, Retardation of droplet motion by surfactant. Part 1. Theoretical development and asymptotic solutions, Chem. Eng. Comm. **20**, 191 (1983).
[26] J. A. Holbrook and M. D. Levan, Retardation of droplet motion by surfactant. Part 2. Numerical solutions for exterior diffusion, surface diffusion, and adsorption kinetics, Chem. Eng. Commun. **20**, 273 (1983).
[27] J. Chen and K. J. Stebe, Marangoni retardation of the terminal velocity of a settling droplet: The role of surfactant physico-chemistry, J. Colloid Interface Sci. **178**, 144 (1996).

[28] Y. Wang, D. T. Papageorgiou, and C. Maldarelli, Increased mobility of a surfactant-retarded bubble at high bulk concentrations, J. Fluid Mech. **390**, 251 (1999).
[29] G. F. Andrews, R. Fike, and S. Wong, Bubble hydrodynamics and mass transfer at high Reynolds number and surfactant concentration, Chem. Eng. Sci. **43**, 1467 (1988).
[30] J. B. Mclaughlin, Numerical simulation of bubble motion in water, J. Colloid Interface Sci. **184**, 614 (1996).
[31] D. M. Leppinen, M. Renksizbulut, and R. J. Haywood, The effects of surfactants on droplet behavior at intermediate Reynolds-numbers. 1. The numerical-model and steady-state results, Chem. Eng. Sci. **51** (1996).
[32] R. B. Fdhila and P. C. Duineveld, The effect of surfactant on the rise of a spherical bubble at high Reynolds and Péclet numbers, Phys. Fluids **8**, 310, (1996).
[33] R. Palaparthi, D. T. Papageorgiou, and C. Maldarelli, Theory and experiments on the stagnant cap regime in the motion of spherical surfactant-laden bubbles, J. Fluid Mech. **559**, 1 (2006).
[34] B. Cuenot, J. Magnaudet, and B. Spennato, The effects of slightly soluble surfactants on the flow around a spherical bubble, J. Fluid Mech. **339**, 25 (1997).
[35] S. Tasoglu, U. Demirci, and M. Muradoglu, The effect of soluble surfactant on the transient motion of a buoyancy-driven bubble, Phys. Fluids **20**, 040805 (2008).
[36] S. Hartland, The profile of the draining film between a rigid sphere and a deformable fluid-liquid interface, Chem. Eng. Sci. **24**, 987 (1969).
[37] S. T. Shah, D. T. Wasan, and R. C. Kintner, Passage of a liquid drop through a liquid-liquid interface, Chem. Eng. Sci. **27**, 881 (1972).
[38] A. F. Jones and S. D. R. Wilson, The film drainage problem in droplet coalescence, J. Fluid Mech. **87**, 263 (1978).
[39] P. G. Smith and T. G. M. Van De Ven, The effect of gravity on the drainage of a thin liquid film between a solid sphere and a liquid/fluid interface, J. Colloid Interface Sci. **100**, 456 (1984).
[40] H. C. Maru, D. T. Wasan, and R. C. Kintner, Behavior of a rigid sphere at a liquid-liquid interface, Chem. Eng. Sci. **26**, 1615 (1971).
[41] A. S. Geller, S. H. Lee, and L. G. Leal, The creeping motion of a spherical particle normal to a deformable interface, J. Fluid Mech. **169**, 27 (1986).
[42] A. N. Srdic-Mitrovic, N. A. Mohamed, and H. J. S. Fernando, Gravitational settling of particles through density interfaces, J. Fluid Mech. **381**, 175 (1999).
[43] N. Abaid, D. Adalsteinsson, A. Agyapong, and R. M. McLaughlin, An internal splash: Levitation of falling spheres in stratified fluids, Phys. Fluids **16**, 1567 (2004).
[44] R. Camassa, C. Falcon, J. Lin, R. M. McLaughlin, and R. Parker, Prolonged residence times for particles settling through stratified miscible fluids in the Stokes regime, Phys. Fluids **21**, 031702 (2009).
[45] R. Camassa, C. Falcon, J. Lin, R. M. McLaughlin, and N. Mykins, A first-principle predictive theory for a sphere falling through sharply stratified fluid at low Reynolds number, J. Fluid Mech. **664**, 436 (2010).
[46] K. Y. Yick, C. R. Torres, T. Peacock, and R. Stocker, Enhanced drag of a sphere settling in a stratified fluid at small Reynolds numbers, J. Fluid Mech. **632**, 49 (2009).
[47] M. Bayareh, A. Doostmohammadi, S. Dabiri, and A. M. Ardekani, On the rising motion of a drop in stratified fluids, Phys. Fluids **25**, 103302 (2013).
[48] A. Doostmohammadi, S. Dabiri, and A. M. Ardekani, A numerical study of the dynamics of a particle settling at moderate Reynolds numbers in a linearly stratified fluid, J. Fluid Mech. **750**, 5 (2014).
[49] H. Hanakazi, K. Kashimoto, and T. Okamura, Jets generated by a sphere moving vertically in a stratified fluid, J. Fluid Mech. **638**, 173 (2009).
[50] H. Hanazaki, K. Konishi, and T. Okamura, Schmidt-number effects on the flow past a sphere moving vertically in a stratified diffusive fluid, Phys. Fluids **21**, 026602 (2009).
[51] H. Hanazaki, S. Nakamura, and H. Yoshikawa, Numerical simulation of jets generated by a sphere moving vertically in a stratified fluid, J. Fluid Mech. **765**, 424 (2015).
[52] L. H. Larsen, Oscillations of a neutrally buoyant sphere in a stratified fluid, Deep-Sea Res. Ocean. Abstr. **16**, 587 (1969).

[53] I. Biró, K. G. Szabó, B. Gyüre, I. M. Jánosi, and T. Tél, Power-law decaying oscillations of neutrally buoyant spheres in continuously stratified fluid, Phys. Fluids **20**, 051705 (2008).
[54] K. Kindler, A. Khalili, and R. Stocker, Diffusion-limited retention of porous particles at density interfaces, Proc. Natl. Acad. Sci. USA **107**, 22163 (2010).
[55] R. Camassa, S. Khatri, R. M. McLaughlin, J. C. Prairie, B. L. White, and S. Yu, Retention and entrainment effects: Experiments and theory for porous spheres settling in sharply stratified fluids, Phys. Fluids **25**, 081701 (2013).
[56] F. Blanchette and A. M. Shapiro, Drops settling in sharp stratification with and without Marangoni effects, Phys. Fluids **24**, 042104 (2012).
[57] C. D. Eggleton and K. J. Stebe, An adsorption-desorption-controled surfactant on a deforming droplet, J. Colloid Interface Sci. **208**, 68 (1998).
[58] H. A. Stone and L. G. Leal, The effects of surfactants on drop deformation and breakup, J. Fluid Mech. **220**, 161 (1990).
[59] B. Lafaurie, C. Nardone, R. Scardovelli, S. Zaleski, and G. Zanetti, Modelling merging and fragmentation in multiphase flows with surfer, J. Comput. Phys. **113**, 134 (1994).
[60] D. L. Brown, R. Cortez, and M. L. Minion, Accurate projection methods for the incompressible Navier-Stokes equations, J. Comput. Phys. **168**, 464 (2001).
[61] S. Popinet and S. Zaleski, A front tracking algorithm for the accurate representation of surface tension, Int. J. Numer. Meth. Fluids **30**, 775 (1999).
[62] D. W. Martin and F. Blanchette, Simulations of surfactant effects on the dynamics of coalescing drops and bubbles, Phys. Fluids **27**, 012103 (2015).
[63] M. Muradoglu and G. Tryggvason, A front-tracking method for computation of interfacial flows with soluble surfactants, J. Comput. Phys. **227**, 2238 (2008).
[64] F. Blanchette and Y. Lei, Energy considerations for multiphase fluids with variable density and surface tension, SIAM Rev. **51**, 423 (2009).
[65] J. C. Padrino, T. Funada, and D. D. Joseph, Purely irrotational theories for the viscous effects on the oscillations of drops and bubbles, Int. J. Multiphase Flow **34**, 61 (2008).
[66] See Supplemental Material at http://link.aps.org/supplemental/10.1103/PhysRevFluids.2.023602 for two drops rising in linear density-stratified ambients: one (left) entrains fluid, while the other (right) does not, because the density has been artificially fixed.